



## Tailored Euler-Lagrange modelling of microfluidic solid/liquid reactive separations

Gloria González-Lavín, Belén García-Merino, Christian Fernández-Maza, Eugenio Bringas, Lucía Gómez-Coma, Marcos Fallanza, Inmaculada Ortiz\*

Departamento de Ingenierías Química y Biomolecular, Universidad de Cantabria, Av. Los Castros s/n, 39005 Santander, Spain

### ARTICLE INFO

#### Keywords:

CFD  
Euler-Lagrange  
Microfluidics  
Reactive separation  
Solid/liquid

### ABSTRACT

Micro- and nano- sized particles display an outstanding performance in the selective capture or release of molecules after the target species is contacted. Microfluidics can hugely benefit the performance of these systems given the remarkable features it presents. In this work, to the best knowledge of the authors, the microfluidic solid/liquid selective interfacial mass transfer is tackled for the first time in a Computational Fluid Dynamics (CFD) model based on the Euler-Lagrange framework. To gain insight on the effect of describing the particles as discrete entities, another model with the same purpose has been developed under the Euler-Euler approach. To experimentally validate and test the performance of the models, the microfluidic capture of chromate ions employing amino-functionalized particles in a Y-Y shaped microdevice has been selected as case study. Both models have been successfully validated, providing a relative root-mean-square error (RRMSE) of 9.86% for the Euler-Lagrange model and 22.62% for the Euler-Euler one. The performance of both models has been tested through a set of simulations in which the residence time and the load of particles are varied. The Euler-Euler option overestimates the hexavalent chromium removal in the kinetic region up to 27.94%, although both provide equally precise equilibrium data. The prediction difference between models is more significant when higher particle loads are used. Therefore, it is concluded that the Euler-Lagrange model proves to be a reliable and highly resourceful tool to predict the behavior of microfluidic multiphase systems in a wide range of conditions.

### 1. Introduction

Solid/liquid particulate systems are increasingly gaining presence in a wide range of applications due to their considerable versatility. Particles can be used as sorbent media in solid phase extraction to recover critical raw materials such as rare earths from different liquid matrices [1], organic pollutants as PAHs, PFAs or BPA [2] or metals like Cd(II), Cr(III), Cr(VI) Hg(II), Pb(II) or As(V) [3,4]. They can also be used with therapeutic purposes through drug delivery [5] and they can catalyze the photodegradation of aqueous pollutants and the photogeneration of hydrogen [6,7]. Microfluidics have proven to offer a fast and reliable platform for such processes in which the precise control of particles fluid dynamics is crucial [8]. Elevated surface-to-volume ratios, reduced handling of both reagents and wastes, decreased diffusional times and tailored passive mixing through the geometry are only a few of the many features that push microfluidics as a promising technology [9–11].

Given the bright path set forward for solid/liquid microfluidic

systems, the availability of a mathematical model that can rigorously predict their functioning giving an insight on the phenomena taking place in the process becomes a critical need. Several options can be considered when facing multiphase systems modelling.

The single-phase, or homogeneous, approach is the simplest option to face the formulation of the problem. In this case, the heterogeneous system consisting of two phases is represented by a set of governing equations referred to a single fluid phase. This simplification implies that both phases present the same properties, the particles show a sufficiently fine size and a uniform distribution through the fluid field and the slip between solid and liquid can be dismissible [12]. This approach has been studied by several authors when describing heat transfer in systems comprising nanofluids. For instance, Minakov et al. [13] developed a single-phase mathematical model to describe fluid dynamics and heat transfer in laminar regime in a forced convection scheme based on CuO nanoparticles. Their model satisfactorily described the experimental data, presenting higher deviations at lower Reynolds numbers. Albojamal et al. [14] built a single-phase model and

\* Corresponding author.

E-mail address: [ortizi@unican.es](mailto:ortizi@unican.es) (I. Ortiz).

<https://doi.org/10.1016/j.cej.2024.153393>

Received 4 March 2024; Received in revised form 11 June 2024; Accepted 20 June 2024

Available online 22 June 2024

1385-8947/© 2024 The Author(s). Published by Elsevier B.V. This is an open access article under the CC BY-NC-ND license (<http://creativecommons.org/licenses/by-nc-nd/4.0/>).

**Nomenclature***Roman symbols*

<b>A</b>	Surface ( $m^2$ )
<b>c</b>	Molar concentration ( $kmol \cdot m^{-3}$ )
<b>C<sub>D</sub></b>	Drag coefficient (–)
<b>C<sub>vm</sub></b>	Virtual mass factor (–)
<b>d</b>	Diameter ( $m$ )
<b>d<sub>ij</sub></b>	Deformation rate tensor ( $s^{-1}$ )
<b>D<sub>i,m</sub></b>	Mass diffusion coefficient of species <i>i</i> in the medium $m$ ( $m^2 \cdot s^{-1}$ )
<b>D<sub>T,i</sub></b>	Thermal diffusion coefficient for species <i>i</i> ( $kg \cdot m^{-1} \cdot s^{-1}$ )
<b>EE</b>	Euler-Euler (–)
<b>EL</b>	Euler-Lagrange (–)
<b><math>\vec{F}</math></b>	Force ( $kg \cdot m \cdot s^{-2}$ )
<b>FD</b>	Functionalization degree ( $kg \cdot kmol^{-1}$ )
<b><math>\vec{g}</math></b>	Gravity vector ( $m \cdot s^{-2}$ )
<b>I</b>	Unit tensor (–)
<b><math>\vec{J}_i</math></b>	Diffusion flux of species <i>i</i> ( $kg \cdot m^{-2} \cdot s^{-1}$ )
<b>k</b>	Equilibrium ratio ( $m^3 \cdot kg^{-1}$ )
<b>k<sub>f</sub></b>	Mass transfer coefficient ( $m \cdot s^{-1}$ )
<b>K</b>	Equilibrium ratio (–)
<b>m</b>	Mass ( $kg$ )
<b><math>\dot{m}_{k,i}</math></b>	Mass flow rate of species <i>i</i> in cell <i>k</i> ( $kg \cdot s^{-1}$ )
<b><math>\dot{m}_{pq}</math></b>	Mass transfer rate from phase <i>p</i> to phase <i>q</i> ( $kg \cdot m^{-3} \cdot s^{-1}$ )
<b><math>\dot{n}_i</math></b>	Molar flow rate of species <i>i</i> ( $kmol \cdot s^{-1}$ )
<b>p</b>	Pressure ( $kg \cdot m^{-1} \cdot s^{-2}$ )
<b>Pe</b>	Peclet number (–)
<b>Q<sub>i,1</sub></b>	Mass fraction of species <i>i</i> on the solid (–)
<b>Re</b>	Reynolds number (–)
<b>RRMSE</b>	Relative Root Mean Squared Error (–)
<b>S<sub>i</sub></b>	Species source term ( $kg \cdot m^{-3} \cdot s^{-1}$ )

<b>S<sub>m</sub></b>	Mass source term ( $kg \cdot m^{-3} \cdot s^{-1}$ )
<b>S<sub>mom</sub></b>	Momentum source term ( $kg \cdot m^{-2} \cdot s^{-2}$ )
<b>Sh</b>	Sherwood number (–)
<b>T</b>	Temperature ( $K$ )
<b><math>\vec{v}</math></b>	Velocity vector ( $m \cdot s^{-1}$ )
<b>V</b>	Volume ( $m^3$ )
<b><math>\vec{x}</math></b>	Position vector ( $m$ )
<b>Y<sub>i</sub></b>	Mass fraction of species <i>i</i> (–)
<i>Greek symbols</i>	
<b>α</b>	Volume fraction (–)
<b>γ</b>	Mass concentration ( $kg \cdot m^{-3}$ )
<b>μ</b>	Dynamic viscosity ( $kg \cdot m^{-1} \cdot s^{-1}$ )
<b>ν</b>	Kinematic viscosity ( $m^2 \cdot s^{-1}$ )
<b>ρ</b>	Density ( $kg \cdot m^{-3}$ )
<b><math>\vec{\tau}</math></b>	Stress tensor ( $kg \cdot m^{-1} \cdot s^{-2}$ )
<b>τ</b>	Residence time ( $s$ )
<b>τ<sub>r</sub></b>	Particle relaxation time ( $s$ )
<b>φ</b>	Molar ratio amino groups per Cr(VI) ( $mol_{amino} \cdot mol_{Cr(VI)}^{-1}$ )

*Subscripts and superscripts*

<b>c</b>	Relative to molar concentration
<b>eq</b>	Relative to the equilibrium
<b>f</b>	Final
<b>i</b>	<i>i</i> -th species
<b>j</b>	<i>j</i> -th species
<b>k</b>	<i>k</i> -th cell
<b>m</b>	<i>m</i> -th medium
<b>p</b>	<i>p</i> -th phase
<b>part</b>	Relative to particle
<b>q</b>	<i>q</i> -th phase
<b>0</b>	Initial
<b>γ</b>	Relative to mass concentration

two two-phase models to describe convective heat transfer and pressure drop of Al<sub>2</sub>O<sub>3</sub> – water nanofluid laminar flow inside a tube. They concluded that the homogeneous model constituted a fast and low-cost tool to analyze nanofluids without the need of heterogeneous models. Maganti et al. [15] developed a computational study employing a single-phase and a two-phase model to analyze concentration and thermohydraulic maldistribution in parallel microchannel systems containing Al<sub>2</sub>O<sub>3</sub> – water nanofluid. Their work pointed out that homogeneous systems are not able to predict nanofluid performance in complex flow geometries, being necessary a two-phase model for that purpose.

To consider in the model the multiphase nature of the particulate microfluidic system, two options arise: Eulerian-Eulerian and Eulerian-Lagrangian models [16]. These two-phase approaches may provide more accurate results since they treat the base fluid and the dispersed solid as individual phases with their own properties, which translates into models with higher complexity requiring longer simulation times to reach a final solution [12]. The Euler-Euler model, also referred to as Two-Fluid Model (TFM), describes both phases as interacting and interpenetrating continua coupled by an interaction term in a fixed reference frame [17]. The concept of volume fraction is introduced to indicate the presence or absence of a phase in time and space. Conservation equations are derived and solved for each phase [18]. This alternative does not consider the solid as a discrete phase, neglecting the position of every particle in time and space. Thus, this reduction in the computational load makes affordable the simulation of denser particulate flows, even for industry-scale systems [19,20]. Nevertheless, some Euler-Euler models devoted to describe solid/liquid flows in microchannels can be found in literature. For example, Amin Arefi et al. [21]

reported a Eulerian model that predicts the deposition of fine nanoparticles on the epithelial layer of a lung-on-a-chip device, being the particulate phase represented by a concentration field. Gracka et al. [22] developed both Euler-Euler and Euler-Lagrange models to predict blood multiphase flow in a microchannel. The authors concluded the need to search for a more rigorous approach that recognizes the discrete nature of the solid phase (in that case, red blood cells) to obtain more accurate velocity and concentration fields.

The Euler-Lagrange approach treats the solid particles as discrete entities, modelled under the Lagrangian moving reference frame. This method tracks the particles along their trajectories by accounting for the relevant forces acting on them. The dispersed phase, conceived as massless points, acts as sources or sinks of mass, momentum and energy in the fluid field. This approach also allows for the use of particles with a size distribution [23,24]. The behavior of the discrete phase can be approached using different models, such as the discrete phase model (DPM), discrete element model (DEM), dense discrete phase model (DDPM) and multiphase particle-in-cell model (MP-PIC). The DPM relies on the concept of “parcels”, which are groupings of real particles with the same properties. This approach is mostly indicated to predict the behavior of particles in dilute flows. DDPM and MP-PIC also track particle parcels, in this case, in dense flows. Both model particle interactions implicitly with the stochastic collision models, although they diverge in the way they treat interparticle interactions. The first one relies on KTGF (Kinetic Theory of the Granular Flow), while the second one uses a solid stress tensor. The DEM considers the shape and properties of each individual particle and models particle-particle interactions employing direct collision models based on a soft-sphere or

hard-sphere approach. This last option is the most computationally demanding [17,25]. Meanwhile, the fluid phase is formulated as a continuum under the Eulerian reference frame. The distinctive features that the Euler-Lagrange approach presents have led to its application in the prediction of the functioning of several and different systems. Erosion [26], absorption [23,27], mixing in stirred tanks [28], virus or infecting particles propagation [29,30], drug deposition [31] or micropollutants photodegradation [32] are just a small sample of the many purposes this approach can handle.

When it comes to microfluidic solid/liquid systems, the Euler-Lagrange approach finds its main task in determining the position of every particle and predicting the heat flow. The first case corresponds with studies whose purpose is to provide a separation extent as a consequence of an applied force or a geometry devised with that mission, to provide beads' deposition degrees or, plainly, to identify the position and distribution of particles along a channel. Magnetic [16,33] or inertial [34,35] propelled separations are some examples. The second case, linked to heat induced migrations, corresponds to the use of nanofluids [36,37]. However, there is scarce evidence of the use of the Eulerian-Lagrangian approach to depict microfluidic solid/liquid interfacial mass transfer.

In light of the ample and long path expected for microfluidic solid/liquid systems in which interfacial mass transfer is involved, a predictive and robust model accounting for the phenomena happening in the device becomes necessary. This work intends to present, to the best knowledge of the authors, the first Eulerian-Lagrangian model devised to stand for the microfluidic capture in solid particles of species dissolved in a liquid phase. To gain insight on the robustness of the model, simulated data for the microfluidic multiphase chromium (VI) capture by amino-functionalized magnetic particles have been compared to experimental values. Furthermore, predictions have been also compared to the information provided with a multiphase simplified model based on the Eulerian-Eulerian approach. The performance of both models is compared under different operational conditions to determine which option is the most convenient in terms of accuracy and solving time.

## 2. Mathematical modelling

Two Computational Fluid Dynamics (CFD) models have been developed, implemented, tested and validated in this work. Both models conceive the feed phase as a continuum, while they treat differently the receptor phase. The Euler-Euler approach describes the particulate receptor phase as another continuous phase. Meanwhile, the Euler-

Lagrange approach considers the solid phase as a discretized set of particles. Therefore, both models present similarities in the description of the fluid phase and specific features in the modelling of the solid one. The two options included in this work aim to predict the capture of a single target species present in the feed phase into the receptor phase (Fig. 1). The two models have been implemented in the software ANSYS FLUENT 2019 R3 (ANSYS, Inc., Canonsburg, PA, USA).

The dynamics of the continuous fluid phase are calculated resorting to the volume-average Navier-Stokes continuity and momentum equations:

$$\frac{\partial}{\partial t} (\alpha_q \rho_q) + \nabla \cdot (\alpha_q \rho_q \vec{v}_q) = \sum_{p=1}^n \dot{m}_{pq} + S_{m,q} \quad (1)$$

$$\begin{aligned} \frac{\partial}{\partial t} (\alpha_q \rho_q \vec{v}_q) + \nabla \cdot (\alpha_q \rho_q \vec{v}_q \vec{v}_q) = \\ = -\alpha_q \nabla \cdot p + \nabla \cdot \bar{\tau}_q + \alpha_q \rho_q \vec{g} + \sum_{p=1}^n \dot{m}_{pq} \vec{v}_{pq} + S_{mom,q} \end{aligned} \quad (2)$$

where  $\alpha (-)$  is the volume fraction of the fluid phase  $q$  in a cell,  $\rho$  ( $\text{kg}\cdot\text{m}^{-3}$ ) is the density,  $\vec{v}$  ( $\text{m}\cdot\text{s}^{-1}$ ) is the velocity vector,  $\dot{m}_{pq}$  ( $\text{kg}\cdot\text{m}^{-3}\cdot\text{s}^{-1}$ ) characterizes the mass transfer rate from phase  $p$  to phase  $q$ ,  $\vec{v}_{pq}$  ( $\text{m}\cdot\text{s}^{-1}$ ) is the interphase velocity,  $p$  ( $\text{kg}\cdot\text{m}^{-1}\cdot\text{s}^{-2}$ ) is the static pressure,  $\vec{g}$  ( $\text{m}\cdot\text{s}^{-2}$ ) is the gravity force.  $S_m$  ( $\text{kg}\cdot\text{m}^{-3}\cdot\text{s}^{-1}$ ) and  $S_{mom}$  ( $\text{kg}\cdot\text{m}^{-2}\cdot\text{s}^{-2}$ ) correspond to the mass and momentum source terms due to the biphasic interaction between continuous and discrete phases, respectively. In addition, the stress tensor  $\bar{\tau}$  ( $\text{kg}\cdot\text{m}^{-1}\cdot\text{s}^{-2}$ ) is given by:

$$\bar{\tau}_q = \mu_q \left[ \alpha_q (\nabla \cdot \vec{v}_q + \nabla \cdot \vec{v}_q^T) - \frac{2}{3} \alpha_q \nabla \cdot \vec{v}_q I \right] \quad (3)$$

Being  $\mu$  ( $\text{kg}\cdot\text{m}^{-1}\cdot\text{s}^{-1}$ ) the viscosity and  $I (-)$  the unit tensor.

To account for the mixing and transport of the chemical species involved in the system, an additional conservation equation describing the effects of convection, diffusional and interfacial mass transfer is considered:

$$\frac{\partial}{\partial t} (\alpha_q \rho_q Y_{i,q}) + \nabla \cdot (\alpha_q \rho_q \vec{v}_q Y_{i,q}) + \nabla \cdot \alpha_q \vec{J}_{i,q} = \sum_{p=1}^n \dot{m}_{p,q}^i + \alpha_q S_{i,q} \quad (4)$$

where  $\vec{J}_i$  ( $\text{kg}\cdot\text{m}^{-2}\cdot\text{s}^{-1}$ ) is the diffusion flux of species  $i$ ,  $\dot{m}_{p,q}^i$  ( $\text{kg}\cdot\text{m}^{-3}\cdot\text{s}^{-1}$ ) denotes the mass transfer source from species  $i$  on phase  $p$

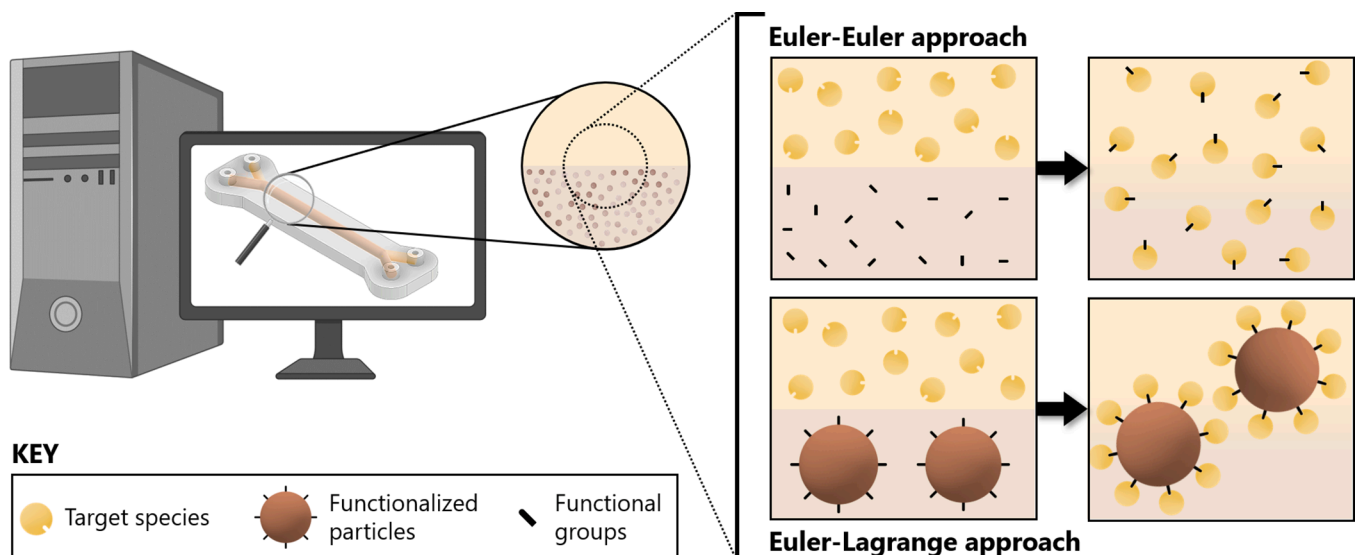


Fig. 1. Schematic diagram of the models' conceptualization.

to species  $j$  on phase  $q$  and  $S_i$  ( $\text{kg}\cdot\text{m}^{-3}\cdot\text{s}^{-1}$ ) is the source term corresponding to species  $i$  due to the interfacial mass transfer with discrete entities. The diffusion flux, which is described through the Fick's law, is expressed as:

$$\vec{J}_{i,q} = -\rho_q D_{i,m} \nabla \cdot Y_{i,q} - D_{T,i} \frac{\nabla \cdot T}{T} \quad (5)$$

where  $D_{i,m}$  ( $\text{m}^2\cdot\text{s}^{-1}$ ) is the mass diffusion coefficient for species  $i$  in the fluid,  $T$  (K) is the temperature and  $D_{T,i}$  ( $\text{kg}\cdot\text{m}^{-1}\cdot\text{s}^{-1}$ ) is the Soret diffusion coefficient. The system is considered to operate under isothermal conditions, so the energy contributions are dismissed.

The Euler-Euler approach conceives both phases as fluid interpenetrating continua. The model includes volume of fluid (VOF) parameters, which introduce the concept of phasic volume fraction ( $\alpha_q$ ), that allows to delineate the interface position. Volume fractions represent the space in a control volume occupied by each phase, being the interphase located in those cells in which the volume fraction varies between 0 and 1 [38]. Eqs. (1) – (5) are solved twice, one for the feed phase and another for the receptor phase.

When the kinetics of the chemical reaction are very fast, it can be considered that the reaction takes place instantaneously at the interface, where the target species reacts with the selective compound. This way, the phenomenon is modelled through a source term for the mass transfer between the two continuous phases:

$$\dot{m}_{p^i q^j} = k_{pq} A (K' \gamma_p^i - \gamma_q^j) \quad (6)$$

being  $A$  ( $\text{m}^2$ ) the interfacial area,  $\gamma_p^i$  ( $\text{kg}\cdot\text{m}^{-3}$ ) the mass concentration of species  $i$  in phase  $p$ ,  $K'$  (–) the mass concentration equilibrium ratio and  $k_{pq}$  ( $\text{m}\cdot\text{s}^{-1}$ ) the overall mass transfer coefficient, which is defined as follows:

$$\frac{1}{k_{pq}} = \frac{1}{k_q} + \frac{K'}{k_p} \quad (7)$$

where  $k_p$  ( $\text{m}\cdot\text{s}^{-1}$ ) and  $k_q$  ( $\text{m}\cdot\text{s}^{-1}$ ) are the phase-specific mass transfer coefficients. In this case,  $k_p$  is modelled as a function of the phase Sherwood number through the Ranz-Marshall model,  $k_q$  is assumed to tend to infinity (as the resistance in the receptor phase is considered null) and  $K'$  is computed through a molar concentration equilibrium ratio  $K^c$  (–), as defined in Eq. (8) [39].

$$c_{q,eq}^j = K^c c_{p,eq}^i \quad (8)$$

Where  $c_{q,e}^j$  ( $\text{kmol}\cdot\text{m}^{-3}$ ) is the molar concentration of species  $j$  in phase  $q$  in equilibrium.

The Euler-Lagrange approach treats the feed phase as a fluid, while the receptor one is described as a discrete phase. Since this model is intended for scenarios with particle dilute flow, the solid phase is modelled under the Discrete Phase Model (DPM) approach, which is valid as long as particle volume fractions inferior to 12% are introduced in the system [40]. Eqs. (1) – (5) describe the fluid phase under a Eulerian fixed framework. The mass, species and momentum coupling between the continuous and discrete phases is achieved through the definition of the so-called source terms, which gather the volume-averaged contributions of all particles in each control volume:

$$S_m = - \sum_k \frac{\dot{m}_k}{V_{cell,k}} \quad (9)$$

$$S_i = - \sum_k \frac{\dot{m}_{k,i}}{V_{cell,k}} \quad (10)$$

$$S_{mom} = - \sum_k \frac{\vec{v}_k \dot{m}_k}{V_{cell,k}} - \sum_{i,k} \frac{\vec{F}_{i,k}}{V_{cell,k}} \quad (11)$$

being  $\dot{m}_k$  ( $\text{kg}\cdot\text{s}^{-1}$ ) the mass flow rate in cell  $k$ ,  $\dot{m}_{k,i}$  ( $\text{kg}\cdot\text{s}^{-1}$ ) the mass flow rate of species  $i$  in cell  $k$ ,  $\vec{F}_{i,k}$  ( $\text{kg}\cdot\text{m}^{-1}\cdot\text{s}^{-2}$ ) force  $i$  in cell  $k$  and  $V_{cell,k}$  ( $\text{m}^3$ ) is the volume of cell  $k$ .

The dispersed solid phase is modelled employing the Lagrangian approach, which tracks every particle by taking into account all the forces exerted on them.

The trajectory of every particle is predicted by integrating the following coupled ordinary differential equations:

$$m_p \frac{d\vec{v}_{part}}{dt} = \sum \vec{F}_T \quad (12)$$

$$\frac{d\vec{x}_{part}}{dt} = \vec{v}_{part} \quad (13)$$

where  $\vec{x}_{part}$  (m) is the position of the particle,  $\vec{v}_{part}$  ( $\text{m}\cdot\text{s}^{-1}$ ) the velocity of the particle,  $m_{part}$  (kg) is the mass of the particle and  $\sum \vec{F}_T$  ( $\text{kg}\cdot\text{m}\cdot\text{s}^{-2}$ ) represents all the relevant external forces with influence on the particles trajectories.

Eq. (12) represents the force balance for each particle, where the left side of the equation accounts for the particle inertia and the right side for the external forces. The model considers the forces gathered on Eq. (14) and itemised on Eqs. (15) – (19).

$$\sum \vec{F}_T = \vec{F}_{drag} + \vec{F}_{buoyancy} + \vec{F}_{virtual\ mass} + \vec{F}_{pressure\ grad.} + \vec{F}_{Saffman\ lift} \quad (14)$$

$$\vec{F}_{drag} = m_{part} \frac{\vec{v} - \vec{v}_{part}}{\tau_r} \quad (15)$$

$$\vec{F}_{buoyancy} = m_{part} \frac{\vec{g}(\rho_{part} - \rho)}{\rho_{part}} \quad (16)$$

$$\vec{F}_{virtual\ mass} = C_{vm} m_{part} \frac{\rho}{\rho_{part}} \left( \vec{v}_{part} \nabla \cdot \vec{v} - \frac{d\vec{v}_{part}}{dt} \right) \quad (17)$$

$$\vec{F}_{pressure\ grad.} = m_{part} \frac{\rho}{\rho_{part}} (\vec{v} \nabla \cdot \vec{v}) \quad (18)$$

$$\vec{F}_{Saffman\ lift} = m_{part} \frac{2K_s \nu^{0.5} \rho d_{ij}}{\rho_{part} d_{part} (d_{ik} d_{kl})^{0.25}} (\vec{v} - \vec{v}_{part}) \quad (19)$$

The virtual mass and the pressure gradient forces are considered in Eq. (14) given that the density ratio between the fluid and the particles is greater than 0.1 [40]. The Saffman's lift force has been regarded since the particles are subjected to low Reynolds numbers [41,42].

In previous equations,  $\tau_r$  (s) is the particle relaxation time, described by Eq. (20),  $\rho_{part}$  ( $\text{kg}\cdot\text{m}^{-3}$ ) represents the density of the particles,  $C_{vm}$  (–) is the virtual mass factor (which receives a value of 0.5),  $K_s$  (–) is the constant coefficient of Saffman's lift force with a value of 2.594,  $\nu$  ( $\text{m}^2\cdot\text{s}^{-1}$ ) is the kinematic viscosity and  $d_{ij}$  ( $\text{s}^{-1}$ ) is a deformation rate tensor [43].

$$\tau_r = \frac{\rho_{part} d_{part}}{18\mu} \frac{24}{C_D Re} \quad (20)$$

Here,  $C_D$  (–) denotes the drag coefficient and  $Re$  is the relative Reynolds number. They can be calculated employing Eqs. (21) and (22), respectively.

$$C_D = a_1 + \frac{a_2}{Re} + \frac{a_3}{Re^2} \quad (21)$$

Where  $a_1$  (–),  $a_2$  (–) and  $a_3$  (–) are constants depending on the Reynolds number [44].

$$Re \equiv \frac{\rho d_{part} \left| \vec{v}_{part} - \vec{v} \right|}{\mu} \quad (22)$$

The particles are assumed to be spherical, rigid, non-rotating and of uniform size.

The interphase mass transfer rates, accounted by the mass and species sources terms given by Eqs. (9) and (10), are calculated using the following equation, assuming that a single species  $i$  is selectively exchanged:

$$\frac{dm_{part}}{dt} = \frac{dm_{part,i}}{dt} = A_{part} k_f \rho (Y_i - Y_{i,1}) \quad (23)$$

$A_{part}$  ( $m^2$ ) is the particle's surface area,  $k_f$  ( $m \cdot s^{-1}$ ) denotes the mass transfer coefficient, while  $Y_i$  (-) and  $Y_{i,1}$  (-) represent the species mass fraction on the bulk of the fluid and at equilibrium with the solid, respectively.

The chemical equilibrium is described as a partition coefficient as follows:

$$Q_{i,1} = Y_{i,1} k_p \quad (24)$$

where  $Q_{i,1}$  (-) is the species mass fraction on the solid and  $k$  ( $m^3 \cdot kg^{-1}$ ), the equilibrium ratio.

The mass transfer coefficient is calculated using the correlation reported by Sirkar [45], which has been developed for small particle Reynold's numbers:

$$Sh = k_f D_i / m d_{part} = 0.992 b^{1/3} Pe^{1/3} \quad (25)$$

here,  $b$  (-) is a parameter depending on the void fraction and  $Sh$  (-) and  $Pe$  (-) are the Sherwood and Peclet dimensionless numbers, respectively.

To account for the interfacial mass transfer, a subroutine coded in C language has been implemented in the ANSYS Fluent software. This submodule tracks the particles over the computational domain and addresses the species interfacial transfer resorting to Eqs. (23) – (25).

The conservation equations for both the feed and receptor phase being modelled under a Euler-Euler and Euler-Lagrange framework are summarized in Table 1.

In the Euler-Euler framework, the pressure-velocity coupling is approached through the phase Coupled SIMPLE (Semi-Implicit Method for Pressure Linked Equations) scheme. The gradient terms are treated employing the least squares cell-based scheme. The convective and diffusive terms are discretized using the first-order upwind scheme.

As for the Euler-Lagrange model, the laminar flow field is solved under steady state conditions employing the pressure-based segregated algorithm SIMPLE. The convective and diffusion terms are discretized

selecting the second-order upwind scheme, while the gradient terms are evaluated using the least squares cell-based scheme. To consider the effect of the interphase contact, the problem is solved following a two-way coupling approach, which implies that the effects of the liquid on the solid and vice versa are considered. Thus, the continuous phase flow is solved without introducing the particulate phase. Once a solution is reached, the discrete phase is approached. To this end, the particle trajectories are computed and the mass and momentum effects resulting from the biphasic interaction are calculated. Next, the liquid phase conservation equations are updated and the particle trajectories, properties and exchange terms are recalculated in the modified continuous flow field iteratively until the convergence criteria is achieved. Fig. 2 depicts the numerical procedure to solve this two-way coupled problem [46].

The boundary conditions for the fluid phases include the normal velocity components at the inlets and atmospheric pressure at the outlets, no-slip condition at the wall side and the corresponding species concentration at the inlets. As for the solid phase, the initial position and velocity of the particles, mass flowrate and species content need to be specified.

The simulations for both models have been run in a workstation equipped with an Intel® Xeon Gold 6148 CPU with 256 GB RAM and 40 physical cores.

### 3. Model testing and experimental validation

Currently, addressing the detection and removal alternatives of persistent pollutants from wastewater stands out as a challenge of major concern. In this context, an emerging technology that is gaining importance in recent years consists of the utilization of functional magnetic particles for solid/liquid separations. Surface-modified particles have been used as magnetic sensors for the detection of harmful substances [47,48] and as adsorbents for the targeted capture of pollutants [49,50]. The properties that make magnetic particles ideal for this kind of applications include their high loading capacity, which facilitates the interaction with target compounds; the ease to be functionalized, that provides selectivity in the interaction; and the superparamagnetic behavior, which appears for particles below a certain material-dependent diameter. Superparamagnetic materials exhibit notably high magnetic saturation values, several orders of magnitude greater than those observed in paramagnetic materials, allowing their efficient separation from complex multiphase systems after application of magnetic fields. Moreover, magnetic particles show chemical stability, high mobility and low intraparticle diffusion rate. This last property results in shorter diffusion distances, reducing the required doses, and faster kinetics in comparison with other conventional adsorbents, lowering the operating costs and increasing the operational efficiency [51–53].

**Table 1**

Conservation equations for the feed phase (FP) and the receptor phase (RP) modelled under the Euler-Euler (EE) and Euler-Lagrange (EL) frameworks.

		EULER-EULER (EE)	EULER-LAGRANGE (EL)
Continuity	FP	$\frac{\partial}{\partial t} (\alpha_F \rho_F) + \nabla \cdot (\alpha_F \rho_F \vec{v}_F) = \sum_{p=1}^n \dot{m}_{pq}$	$\frac{\partial}{\partial t} \rho + \nabla \cdot (\rho \vec{v}) = S_m$
	RP	$\frac{\partial}{\partial t} (\alpha_R \rho_R) + \nabla \cdot (\alpha_R \rho_R \vec{v}_R) = \sum_{p=1}^n \dot{m}_{pq}$	$\frac{dm_{part}}{dt} = A_{part} k_f \rho (Y_i - Y_{i,1})$
Momentum	FP	$\frac{\partial}{\partial t} (\alpha_F \rho_F \vec{v}_F) + \nabla \cdot (\alpha_F \rho_F \vec{v}_F \vec{v}_F) = -\alpha_F \nabla \cdot p + \nabla \cdot \vec{\tau}_F + \alpha_F \rho_F \vec{g} + \sum_{p=1}^n \dot{m}_{pq} \vec{v}_{pq}$	$\frac{\partial}{\partial t} (\rho \vec{v}) + \nabla \cdot (\rho \vec{v} \vec{v}) = -\nabla \cdot p + \nabla \cdot \vec{\tau} + \rho \vec{g} + S_{mom}$
	RP	$\frac{\partial}{\partial t} (\alpha_R \rho_R \vec{v}_R) + \nabla \cdot (\alpha_R \rho_R \vec{v}_R \vec{v}_R) = -\alpha_R \nabla \cdot p + \nabla \cdot \vec{\tau}_R + \alpha_R \rho_R \vec{g} + \sum_{p=1}^n \dot{m}_{pq} \vec{v}_{pq}$	$m_{part} \frac{d\vec{v}_{part}}{dt} = \sum \vec{F}_T$
Species	FP	$\frac{\partial}{\partial t} (\alpha_F \rho_F Y_{i,F}) + \nabla \cdot (\alpha_F \rho_F \vec{v}_F Y_{i,F}) + \nabla \cdot \alpha_F \vec{J}_{i,F} = \sum_{p=1}^n \dot{m}_{p,i}$	$\frac{\partial}{\partial t} (\rho Y_i) + \nabla \cdot (\rho \vec{v} Y_i) + \nabla \cdot \vec{J}_i = S_i$
	RP	$\frac{\partial}{\partial t} (\alpha_R \rho_R Y_{i,R}) + \nabla \cdot (\alpha_R \rho_R \vec{v}_R Y_{i,R}) + \nabla \cdot \alpha_R \vec{J}_{i,R} = \sum_{p=1}^n \dot{m}_{p,i}$	$\frac{dm_{part,i}}{dt} = A_{part} k_f \rho (Y_i - Y_{i,1})$

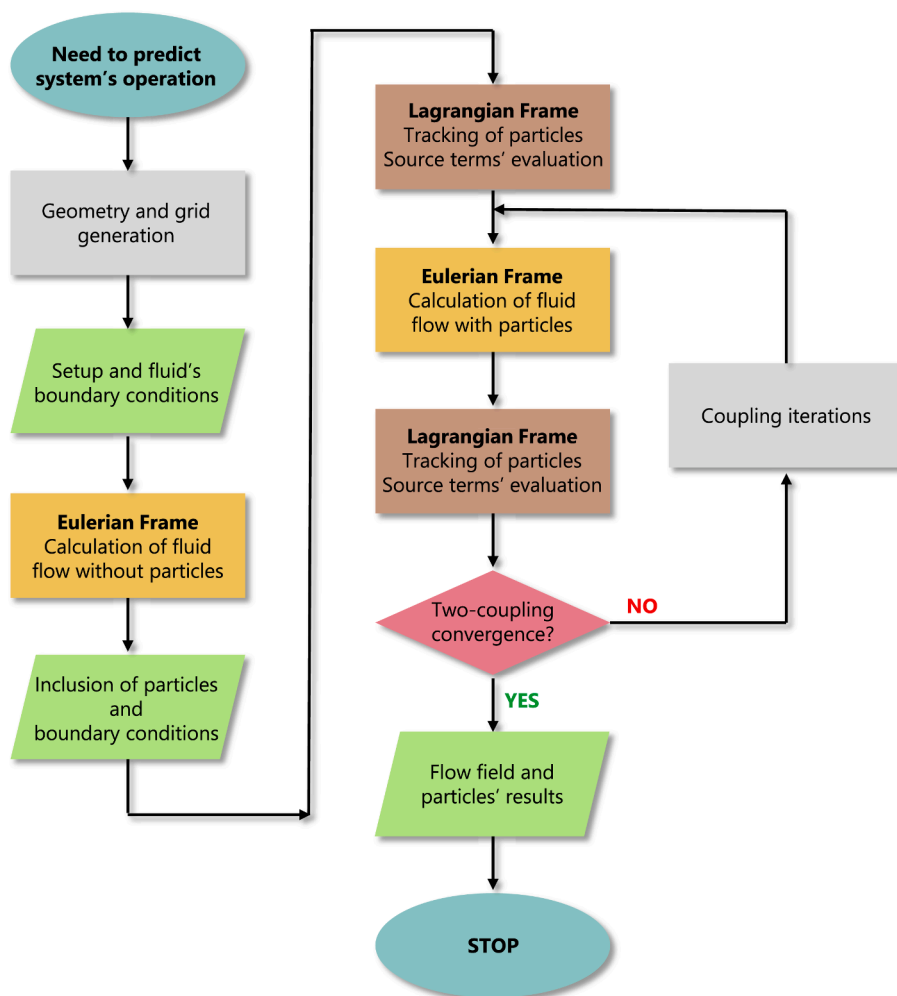


Fig. 2. Flowchart depicting the numerical procedure to solve the two-way coupled model.

Once the beads are synthesized and properly functionalized, it is important to test their behavior for the target environmental application. To this end, the use of microfluidics appears as a promising technology. Microdevices operate under the laminar regime, handle short residence times and offer a favorable high area/volume ratio, improved kinetics for mass and heat transfer, the capability to operate in continuous mode and the possibility of greatly enhance the mixing by designing a proper geometry, preventing agglomeration and adhesion of the particles to the walls [10,39]. The magnetophoretic recovery of magnetic particles from complex fluids using microdevices has been deeply studied both experimentally and by means of mathematical models [33,54,55]. However, there is scarce information about the capture stage. In 2022, a previous work of the research group used a microfluidic device to test the behavior of amino-functionalized magnetic particles for the capture of pollutants from aqueous solutions, using Cr(VI) as model compound [4]. The current work evaluates the feasibility of Euler-Euler and Euler-Lagrange models to rigorously describe the phenomena responsible for the said case of study.

The geometry used in the simulations of Cr(VI) capture is shown in Fig. 3. It consists of a Y-Y microfluidic device with two inlets, two outlets, a circular section of 3 mm diameter and a length of 50 mm. This type of straight channel has been selected to study the performance of both models in absence of passive mixing [9,11]. The microdevice was meshed with a regular grid using a multizone method with a higher refinement in the radial direction. Both models considered that an aqueous solution of 0.44 mM of Cr(VI) was introduced through the upper inlet. In the case of the Euler-Euler model, amino solutions in the

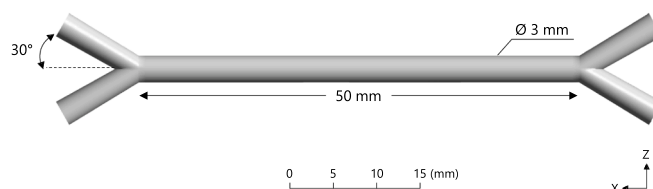


Fig. 3. Microdevice geometry and dimensions.

range 0.44 – 1.32 mM were introduced through the lower inlet, while for the Euler-Lagrange model, suspensions of micrometric particles in the range 2.5–8 g·L<sup>-1</sup> with an amino functionalization level of  $1.7 \times 10^{-4}$  mol<sub>amino</sub>·g<sub>part</sub><sup>-1</sup> were employed. The applied ratio of moles of the amino functional group per moles of hexavalent chromium,  $\phi$  (-), was calculated using Eq. (26), where  $c_{Cr(VI)}$  (mol<sub>Cr(VI)</sub>·L<sup>-1</sup>) is the initial molar concentration of the prepared chromium (VI) solution and  $c_{part}$  (mol<sub>amino</sub>·L<sup>-1</sup>) is the molar concentration of the amino functional groups in the suspension of particles. This last value is obtained from the mass concentration of the suspension of particles ( $\gamma_{part}$ , g·L<sup>-1</sup>) and the calculated functionalization degree of the particles ( $FD$ , mol·g<sup>-1</sup>).

$$\phi = \frac{c_{part}}{c_{Cr(VI)}} = \frac{FD \cdot \gamma_{part}}{c_{Cr(VI)}} \quad (26)$$

Thus, both in Euler-Euler and Euler-Lagrange simulations, the ratio between amino groups and Cr(VI) was in the range 1–3 mol<sub>amino</sub>·mol<sub>Cr</sub>

(VI)<sup>-1</sup>. Table 2 shows the concentration of chromium (VI) capturing agents employed for each model.

The system was considered to operate under room temperature (20 °C) and the density and viscosity of the fluid phases were assigned the values of 998.2 kg·m<sup>-3</sup> and 10<sup>-3</sup> cP, respectively. Furthermore, the diffusion coefficient of chromate ions in water was set as 1.76 × 10<sup>-9</sup> m<sup>2</sup>·s<sup>-1</sup> [39].

Experiments were performed under acidic pH conditions, at which Cr (VI) is present in the form of bichromate. As a result, the mechanism of hexavalent chromium removal takes place due to an ion exchange reaction between bichromate anions and the primary and secondary protonated amino groups, as shown in (R1).



This chemical reaction takes place instantaneously at the interphase, and the phenomena is included in the Euler-Euler model by means of the molar concentration equilibrium ratio  $K^c$  previously defined in Eq. (8). The values of this constant for the different mol<sub>amino</sub>·mol<sub>Cr(VI)</sub><sup>-1</sup> ratios are calculated by means of Eq. (27), where  $K_{eq}$  is the equilibrium constant calculated from experimental data obtained in a previous work [4];  $[Cl^-]$  is the equilibrium chloride concentration in the solution, considered equal to the captured chromate concentration  $[NH_n^+ \cdot HCrO_4^-]$ , assuming the stoichiometric ratio 1:1; and finally,  $[NH_n^+ \cdot Cl^-]$  is the concentration of chloride groups on the particles at equilibrium, calculated after the mass balance to the known concentration of functional groups on the surface of the beads and the calculated chloride equilibrium concentration in solution.

$$K^c = K_{eq} \cdot \frac{[Cl^-]}{[NH_n^+ \cdot Cl^-]} \quad (27)$$

In the case of the Euler-Lagrange approach, the chromium (VI) distribution between both phases is taken into account through Eq. (24), where  $k$  has a value of 0.49 m<sup>3</sup>·kg<sup>-1</sup>. This equilibrium ratio value is calculated starting from equilibrium data obtained in a preceding work [4], which reports the extent of hexavalent chromium capture for different loads of particles.

All chemicals employed in the experimental validation were used as received without further purification and all solutions were prepared with ultrapure water (18 MΩcm, MilliQ, Milipore). Ferrous chloride (FeCl<sub>2</sub>·4H<sub>2</sub>O, ≥99%), ferric chloride (FeCl<sub>3</sub>·6H<sub>2</sub>O, ≥99%), n-[3-(trimethoxysilyl) propyl] ethylenediamine (TMPEd, 99%), sodium hydroxide (NaOH 2 M) and hydrochloric acid (HCl, 2 M) were purchased from Sigma-Aldrich. Isopropyl alcohol (C<sub>3</sub>H<sub>8</sub>O, 99.5%) was obtained from PanReac AppliChem, and ethanol (C<sub>2</sub>H<sub>5</sub>OH, ≥99.5%) was provided by Merck. Finally, potassium chromate (K<sub>2</sub>CrO<sub>4</sub>) was purchased from Scharlau.

The magnetic particles made of magnetite were continuously synthesized and continuously functionalized with amino groups, following a method previously reported by the research group [4]. Briefly, a 0.1 M Fe solution and a 0.57 M NaOH solution were introduced in a spiral-shape PLA microreactor, which was submerged in a thermal bath at 60 °C; applying a residence time of 2 min 40 s, the beads were collected at the outlet, centrifuged, separated from the supernatant with the help of a magnet, washed with ethanol and dried in the oven. The aim of the

functionalization was to anchor primary and secondary amino groups on the surface of the particles; in this case, a suspension of 5000 mg<sub>part</sub>·L<sup>-1</sup> and a solution of 9 × 10<sup>-2</sup> M TMPEd were introduced in the spiral-shape microreactor at ambient temperature with a residence time of 4 min; functional particles were collected at the outlet, centrifuged, separated from the supernatant with the help of a magnet, washed with iso-propyl alcohol and dried in the oven. Thus, spherical particles with amino-functionalization in the order of 10<sup>-4</sup> mol<sub>amino</sub>·g<sub>part</sub><sup>-1</sup> were obtained. The complete characterization of these particles was presented in a previous work [4].

For the ion exchange reactive capture of Cr(VI) as seen in (R1), the amino-functionalized solids have to be protonated. Therefore, HCl was applied to protonate the primary and secondary amino groups in the surface of the functionalized particles, as presented in (R2). A solution of 0.01 M HCl was added to the particles with a ratio of 500 mL·g<sub>part</sub><sup>-1</sup>; the resulting suspension was sonicated for 5 min and left stirring for 6 h at ambient temperature; when the reaction ended, particles were centrifuged, separated from the supernatant with the help of a magnet, washed with ultrapure water and put in the oven until completely dried.



For the Cr(VI) capture experiments, the previously described Y-Y microdevice (Fig. 3), was made of PLA using an Ultimaker S3 3D printer. Tetrafluoroethylene tubing (0.3 mm ID and 1.58 mm OD) was used to connect the microreactor with a pressure pump (Asia Flow Chemistry Syringe Pump, Syrris). Experiments were performed at ambient temperature, working in continuous mode with the previously described microdevice. To this end, a 0.44 mM chromium (VI) solution with a pH of 7.25 was introduced in the upper inlet while a suspension of particles containing 1.32 mM concentration of amino groups in the surface of the particles and a pH of 2.74 was pumped through the lower inlet. Fig. 4 depicts the experimental setup. The contact between both phases took place continuously inside the microfluidic device with flowrates ranging between 6.24 to 424 μL·min<sup>-1</sup> per inlet. The upper and lower streams were collected at the two outlets respectively, samples were centrifuged, the magnetic particles were separated with the help of a magnet and the supernatant was analysed using microwave plasma atomic emission spectroscopy in an MP-AES Agilent spectrometer at a wavelength of 427.48 nm. Experiments were duplicated to prove reproducibility, and thus, results are shown as mean values ± their standard deviation.

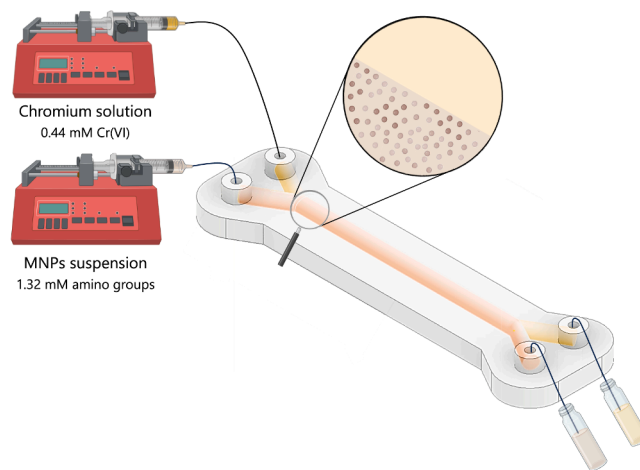


Fig. 4. Setup for the experimental microfluidic capture of Cr(VI).

Table 2  
Concentration of chromium (VI) capture agents employed in the simulations.

	Concentration of particles (g·L <sup>-1</sup> )	Concentration of amino groups (mM)	Number of particles
$\phi = 1$	2.5	0.44	3.22 × 10 <sup>8</sup>
$\phi = 3$	8	1.32	1.03 × 10 <sup>9</sup>

## 4. Results

### 4.1. Analysis of grid independence

First, a grid independence study was carried out to test the quality of the mesh to be employed in the simulations described along this work. For that purpose, five meshes with a number of nodes in the range  $10^4 - 2.16 \times 10^5$  were evaluated, for both models, in terms of hexavalent chromium capture, as defined by Eq. (28), setting a residence time of 300 s and a value of  $\phi$  of 1. Fig. 5 shows the dependence of the Cr(VI) capture on the mesh refinement, being noticeable that above  $6.6 \times 10^4$  nodes the increase in the computational cost does not have a significant relevance on the capture of the target species. Hence, a grid containing  $6.6 \times 10^4$  nodes was selected and employed in the simulations described in the following lines.

$$\text{Capture Cr(VI) (\%)} = \frac{\dot{n}_{\text{Cr(VI)},0} - \dot{n}_{\text{Cr(VI)},f}}{\dot{n}_{\text{Cr(VI)},0}} \cdot 100 \quad (28)$$

Where  $\dot{n}_{\text{Cr(VI)},0}$  ( $\text{kmol}\cdot\text{s}^{-1}$ ) stands for the initial chromate molar flow rate and  $\dot{n}_{\text{Cr(VI)},f}$  ( $\text{kmol}\cdot\text{s}^{-1}$ ), for that one leaving the system.

### 4.2. Model validation

The reliability of the Euler-Euler and Euler-Lagrange based models has been tested from the comparison with experimental values, as represented in Fig. 6.

As shown in Fig. 6, both models are able to adequately predict the multiphasic capture phenomena with absolute deviations inferior to

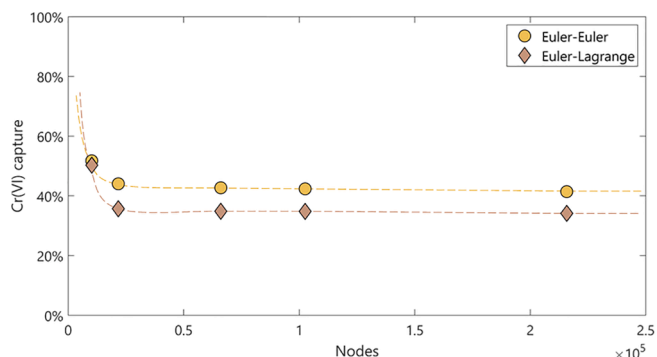


Fig. 5. Grid independence test. Dashed lines have been included to guide the eye.

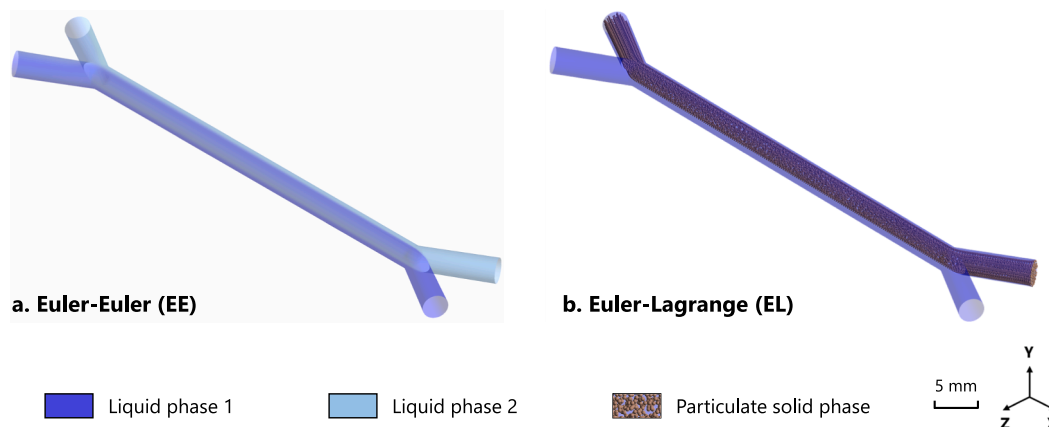


Fig. 7. Diagram showing the phases treatment in the simulations carried out using the a) Euler-Euler and b) Euler-Lagrange models.

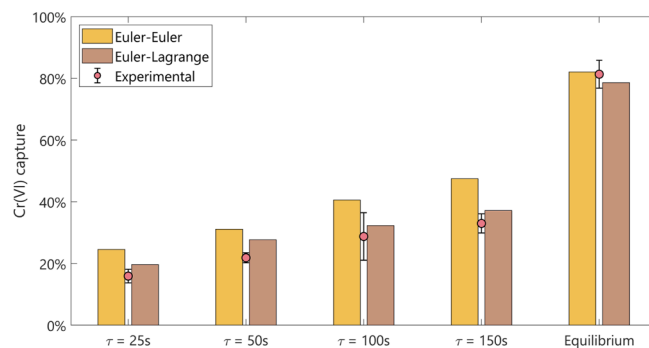


Fig. 6. Comparison between experimental and modelled data with a  $\phi$  value of 3.

15% in the case of the Euler-Euler approach and 6% in the case of the Euler-Lagrange one. The accuracy of both models has been compared in terms of their relative root-mean-square error, RRMSE (–), which quantifies the differences between predicted and observed values and scales these residuals with the observed data:

$$\text{RRMSE} = \sqrt{\frac{\frac{1}{n} \sum_{i=1}^n (y_i - \hat{y}_i)^2}{\sum_{i=1}^n (\hat{y}_i)^2}} \quad (29)$$

Attending to this parameter, the model accuracy can be considered excellent when  $\text{RRMSE} < 10\%$ , good if  $10\% < \text{RRMSE} < 20\%$ , fair if  $20\% < \text{RRMSE} < 30\%$  and poor when  $\text{RRMSE} > 30\%$  [56]. In this case, the Euler-Euler based model presents a RRMSE of 22.62%, while the model relying on the Euler-Lagrange approach displays a RRMSE of 9.86%. Both models can precisely predict equilibrium data with a deviation inferior to 2.5%.

### 4.3. Comparison of the results obtained with Euler-Euler (EE) and Euler-Lagrange (EL) models

The crucial difference between the two approaches studied in this work lies on the description of the fluid dynamics of the particles, namely, the receptor phase. While EE model omits the presence of discrete solid entities, EL model considers it (Fig. 7). This is a key feature that determines the simulated results of system operation.

The performance of the two models is studied attending to the hexavalent chromium capture they provide using different  $\phi$  values, maintaining a constant Cr(VI) initial concentration of 0.44 mM. The

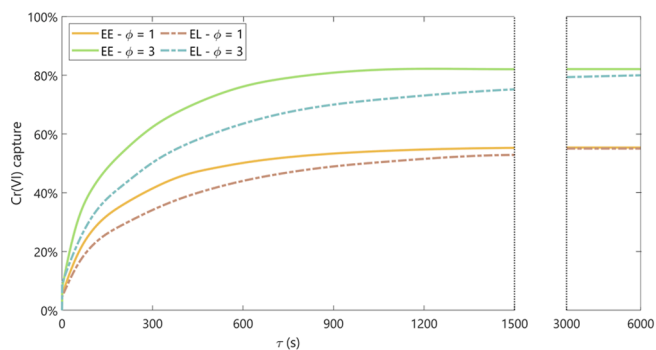


Fig. 8. Euler-Euler and Euler-Lagrange predicted chromium (VI) capture at different  $\phi$  values.

results depicted in Fig. 6 and Fig. 8 show that the Euler-Euler approach leads to a capture overestimation before the chemical equilibrium is reached. The capture is governed by (R1). Hence, for the capture to happen, the chromate ions and the amino groups, in the case of the Euler-Euler approach, and the chromate ions and the particles, in the case of the Euler-Lagrange approach, need to get in contact. In both approaches the mobility of the Cr(VI) species depends on their diffusivity in the liquid medium. However, the mobility of the amino groups is addressed differently in each model. The Euler-Euler alternative treats them as species with a defined diffusivity, while the Euler-Lagrange model considers that the Cr(VI) species are attached to the injected particles, whose movement is determined by the force balance. Therefore, the contact between the reacting species is simplified in the first case, leading to a superior chromium (VI) capture. The discrepancy between both approaches becomes more significant at low residence times (reaching capture overestimations up to 27.94% for residence times inferior to 600 s), while it is softened as the capture system approaches chemical equilibrium, attaining practically the same values

when both entities are given enough time to get in contact.

This deviation turns more noticeable when the ratio between amino groups and chromium (VI) ( $\phi$ ) increases, which implies raising the concentration of particles. The higher the molar ratio between amino groups and chromate, the higher is the divergence of the models in predicting the capture of chromium (VI). Fig. 9 shows simultaneously the effect of the particle concentration and the residence time on the Cr (VI) removal. Warmer colors point to higher removal percentages, being perceptible that, for the same conditions, the simplified multiphasic model (Fig. 9a.) provides values superior to the ones predicted by the fully heterogeneous option (Fig. 9b.) Thus, the Euler-Euler option presents a simplification in the mass transfer opposed to the more rigorous consideration that the Euler-Lagrange alternative pays to the fluid dynamics of the particles, which affects the prediction of the evolution of the system in the kinetic region.

The capture extent provided by each model can also be analyzed through the contour plots to a transversal plane of the Y-Y device (Fig. 10) for operational times comprised in the kinetic region. The presence of Cr(VI) in the liquid phase is presented in a scale of colors that varies from red (maximum Cr(VI) concentration) to blue (minimum Cr (VI) concentration). Fig. 10a., b., e. and f. depict the influence of the residence time when employing a  $\phi$  value of 1, as predicted by the EE and EL models. The contour plots for the shorter residence time (100 s), show how the effect of diffusivity is more limited for short operational times, leading the species to follow a distribution resembling the parallel flow development that is characteristic in microfluidics. The principal exchange of species is taking place at the interphase (central axis of the device). When increasing the residence time up to 400 s, diffusion has already started to have a noteworthy contribution to mass exchange. Around half the length of the channel, the fluids begin to present green tonalities that spread to the total width of the reactor. Therefore, the increased Cr(VI) capture is responding to a chained mechanism between diffusion and the chemical reaction. Moreover, at low residence times (higher flowrates) the predicted outcomes for the EE (Fig. 10 a) and the

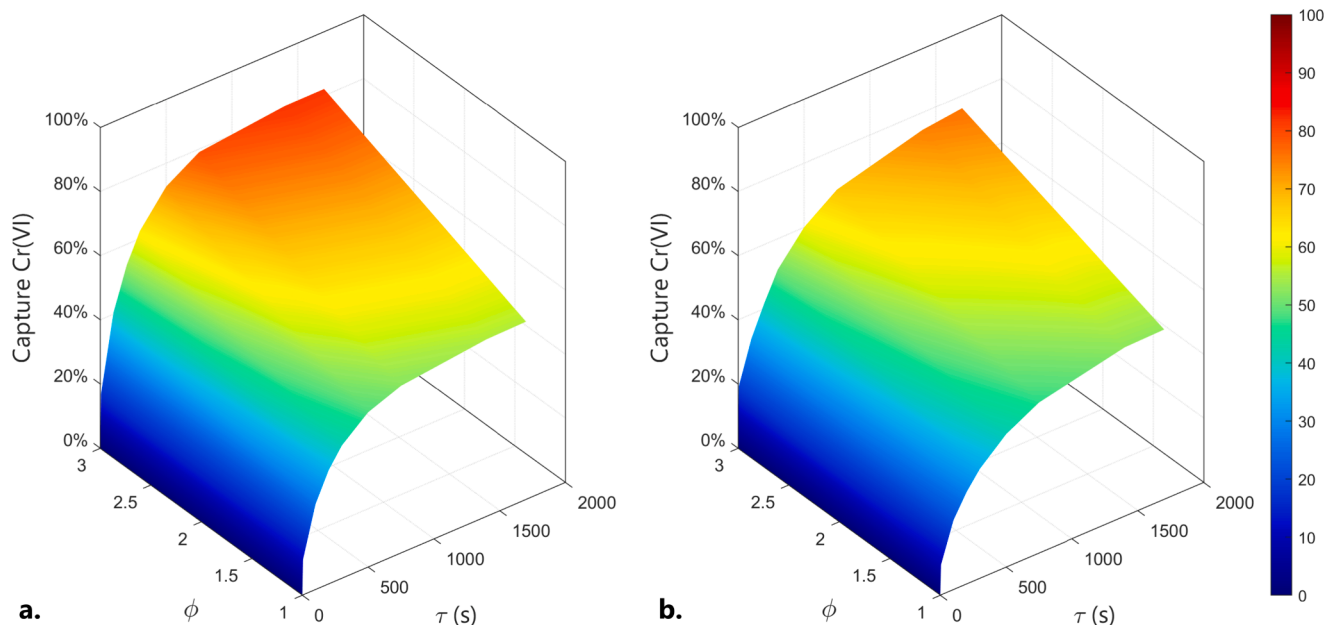


Fig. 9. Effect of particle concentration and residence time on the chromium (VI) removal as predicted by a. the Euler-Euler based model and b. the Euler-Lagrange one.

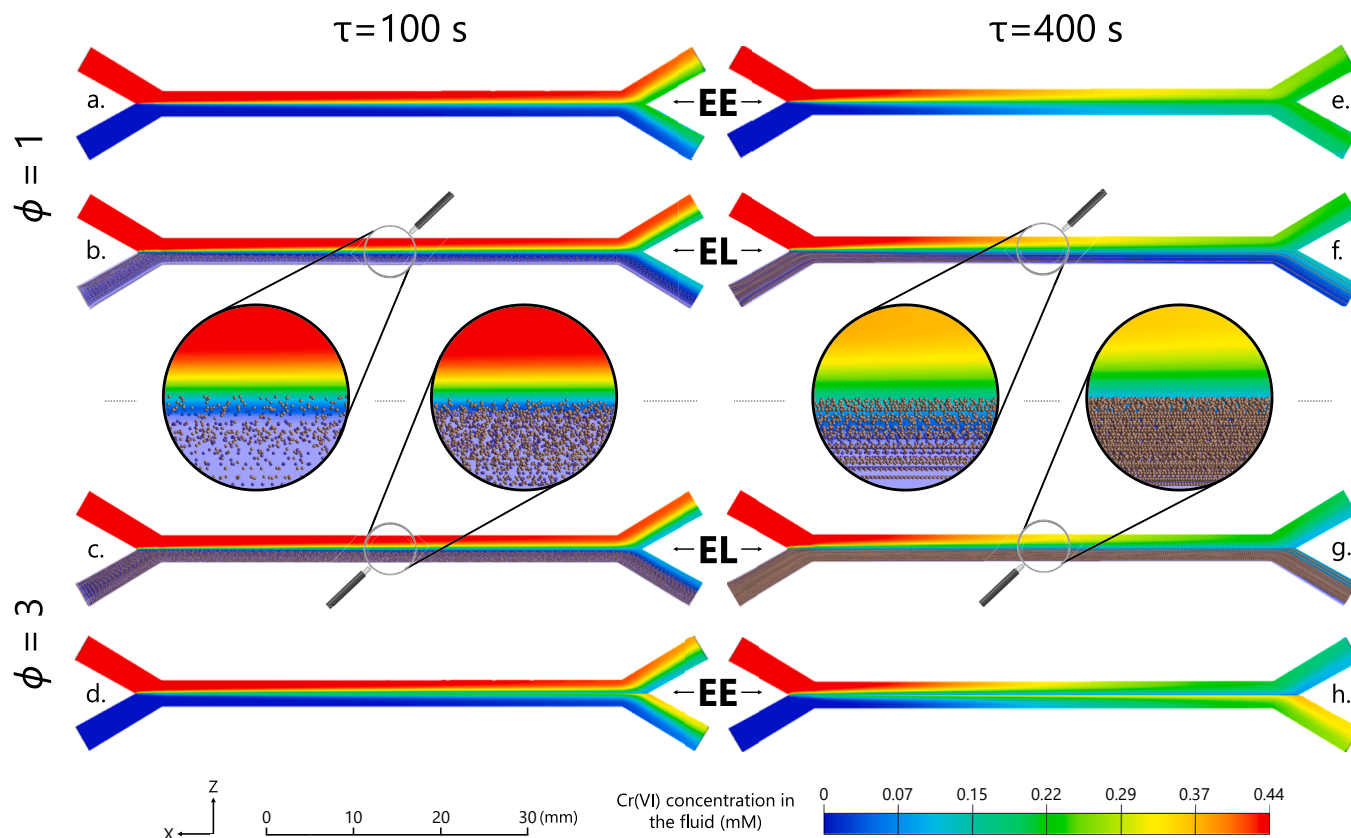


Fig. 10. Contour plots showing the chromium (VI) removal in the feed phase (liquid). Results are shown for both models for a residence time of 100 s and 400 s and for 1 and 3 as  $\phi$  values. Solid particles are scaled 500:1 for visualization.

EL models (Fig. 10 b) are quite resemblant. However, it can be observed that, at the lower outlet of the device, the EE contour presents a greener color, connected with a superior capture. For a residence time of 400 s, the upper outlet for the EL option (Fig. 10f.) shows a bluer tonality in the upper outlet, although the capture result is lower than in the Euler-Euler case (Fig. 10e.), which is more yellowish. In this case, the difference is not due to the capture of Cr(VI), but to differences related to the formulation of the models.

Analogously, Fig. 10c., d., g. and h. show how rising  $\phi$  to 3 affects the system for the same residence times (100 and 400 s), as predicted by the EE and EL models. Increasing the concentration of particles leads to higher Cr(VI) removals (the upper outlets of the aforementioned contours are bluer than those for an  $\phi$  of 1). Again, the effect of the residence time is clearly recognizable. Moreover, the upper outlet shows bluer tonalities in the case of the EE model for both residence times, implying a lower concentration of Cr(VI) or, what is the same, a superior Cr(VI) removal. In all the studied cases, the closer the system is to the equilibrium conditions, the smoother is the increase in the capture when any variable is modified to favor the equilibrium.

In the central axis of Fig. 10, images of the flow of particles at half of the channel are gathered for the two residence times and  $\phi$  values. Larger concentration of particles and lower flowrates lead to higher particle densities, being related to the amount of solid in the first case and to their accumulation in the second. To extend the analysis on the Cr (VI) capture by the particles, plots of the solids at different locations of the device showing the Cr(VI) mass fraction are assembled in Fig. 11. Particles with a null loading of Cr(VI) are colored in blue. As the

captured Cr(VI) attached to the particles increases, their color shifts to lighter blues, green and yellow (as shown in the scale provided in Fig. 11).

The higher the time and  $\phi$  values, the more obvious it is the color shift in the particles, related to a superior Cr(VI) uptake by the particles. If the pictures are analyzed by pairs for the same residence time (Fig. 11a. with Fig. 11b. and Fig. 11c. with Fig. 11d.), it can be appreciated that the particles for the case with lower  $\phi$  (Fig. 11a. and Fig. 11b.) are reaching higher mass fractions of Cr(VI), as the colors for the surroundings of the central axis of the outlet (interphase) are approaching yellowish greens, while the case with higher  $\phi$  (Fig. 11c. and Fig. 11d.) is stuck on tonalities approaching blue and greenish blues. For the same capture of Cr(VI) referred to the aqueous phase, the higher the functionalization degree of the particles (larger  $\phi$ ), the lower is going to be the Cr(VI) mass fraction in the solid particles. For that reason, it may appear that the cases with lower  $\phi$  capture more Cr(VI) because they display higher Cr(VI) mass fractions in the particles. However, when higher  $\phi$  are used, although the mass fraction of Cr(VI) in the solid may be more diluted, the global uptake referred to the aqueous phase is superior. Fig. 11c. depicts the case in which the particles are being leveraged the most, as the lower load and higher residence times allow each individual particle to capture more Cr(VI) (this does not lead to a superior global capture). Fig. 11 shows that the hexavalent chromium capture takes place mainly in the surroundings of the interphase, being less noticeable at more distant points. Fig. 12 is built to probe the hexavalent chromium capture spatial extent that the Euler-Euler model predicts.

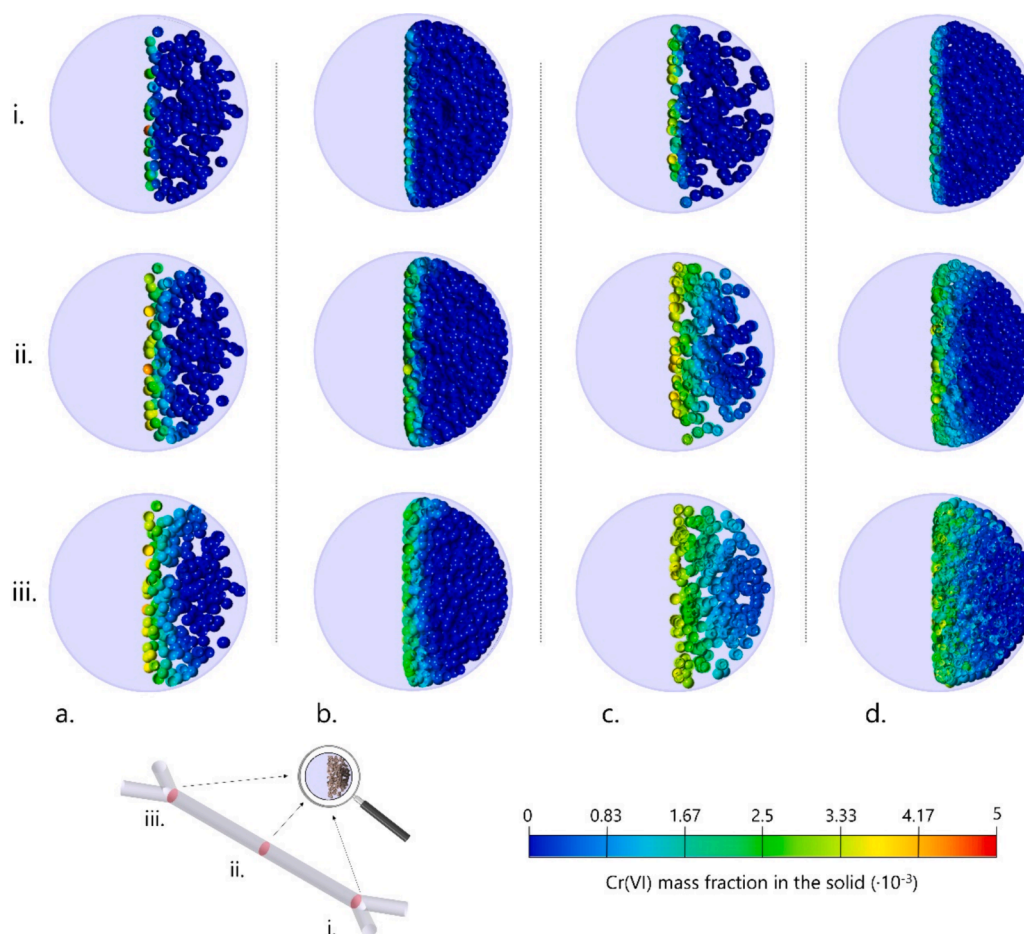


**Fig. 11.** Plots showing the chromium (VI) mass fraction on the particles at the i. inlet, ii. half and iii. outlet of the device for the following operational conditions: a.  $\tau = 100$  s and  $\phi = 1$ ; b.  $\tau = 100$  s and  $\phi = 3$ ; c.  $\tau = 400$  s and  $\phi = 1$  and d.  $\tau = 400$  s and  $\phi = 3$ . Solid particles are scaled 1500:1 for visualization.

At the very inlet, it can be seen in Fig. 12i. that the EE model already presents less Cr(VI) in the feed phase (left half of the circle), while the receptor phase is gaining more Cr(VI) compared to the outcomes brought by the EL option. When advancing in the channel, the difference is still recognizable, endorsing the fact that the simplified model leads to higher removals due to an easiness in the species mobility.

The divergences between models do not only comprise physico-chemical features attained to the microfluidic system that is being evaluated, they also play a key role in the operation of the models themselves. In the first place, the Euler-Euler based alternative considers both phases as two fluids. Therefore, there is no need to define a solid particulate phase that exchanges species with the fluid one when they get into contact. In the case of the Euler-Lagrange option, with the software selected for this purpose, the interfacial mass transfer had to be implemented to the software via a subroutine, coded separately.

As for the running of simulations, convergence issues and computational time are two important details to take into account. The simulations concerning both models have been run in the same equipment with the same processes. In the case of the Euler-Euler alternative, the simulations have been straight forward and notably short. However, in the case of the Euler-Lagrange option, run under a two-coupling scheme, convergence is an important bottle neck that has to be faced, especially when increasing the concentration of particles. The under-relaxation

factors are a good ally to tackle this issue. However, decreasing the last ones leads to increasing notably the computational time, so the use of the Euler-Lagrange model sets the need to find a tradeoff between reaching convergence and increasing the computational time, which is a non-existing limitation in the Euler-Euler case.

When resorting to multiphase models, it is important to have both phases tracked down. In the selected case study, the capture of hexavalent chromium is approached with functionalized magnetic particles because their recovery is guaranteed with the use of magnets. Therefore, there is an interest on separating both phases after the mass transfer between them has occurred. It is unfeasible for the Euler-Euler model to predict whether the particles are going to be separated from the liquid when a magnetic field is applied or whether the hydrodynamic force has diverted them to one location or another. However, the separation of phases can be implemented to the Euler-Lagrange model, making it an even more versatile tool.

Thus, both models present a series of advantages and disadvantages (Table 3). They have proven to be resourceful and highly valuable tools to predict the behavior of microfluidic solid/liquid systems in which interphase mass transfer driven by chemical reactions is involved. The Euler-Euler based option is optimal to provide capture data in the proximity of chemical equilibrium in a fast and reliable way. The Euler-Lagrange model constitutes a robust option that can predict the behavior

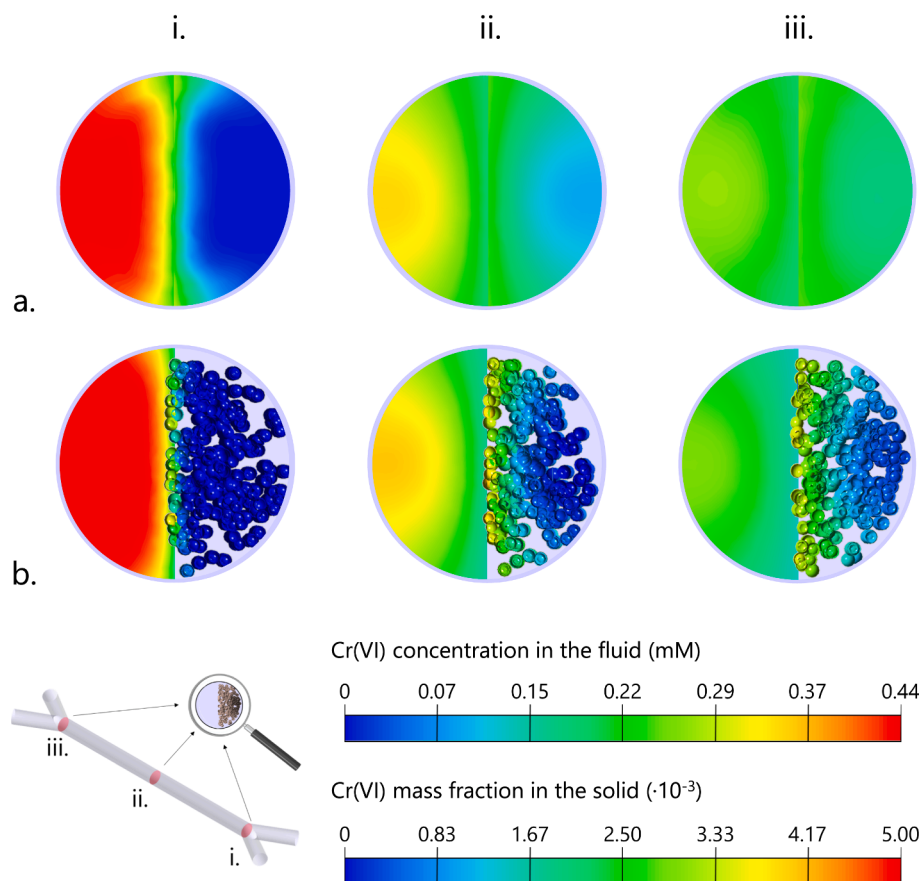


**Fig. 12.** Plots showing the chromium (VI) presence in the feed phase (left halves) and receptor phase (right halves) at the i. inlet, ii. half and iii. outlet of the device for  $\tau = 400$  s and  $\phi = 1$  as predicted by the a. Euler-Euler model and b. Euler-Lagrange model. Solid particles are scaled 2000:1 for visualization.

**Table 3**

Summary of the strong points of each of the considered models.

		Euler-Euler	Euler-Lagrange
Predicted data quality	Kinetic data		X
	Equilibrium data	X	X
Model operation	Implementation easiness	X	
	Convergence easiness	X	
	Solving time	X	
Assembling with phase separation approaches			X

of the system in any conditions and that can be integrated with other stages of the system to give place to a model that overlooks the whole operation of a system.

## 5. Conclusions

In this work, to the best knowledge of the authors, the first model based on the Eulerian-Lagrangian framework for the prediction of the fluid dynamics and interfacial mass transfer and chemical reaction between liquid and solid particles is reported. This model takes into consideration the solid particles as discrete entities and follows their trajectories along time and space. To give a deeper insight on the importance of modelling the solid phase recognizing its individual nature, a Euler-Euler model has been also developed with the objective of predicting the mass transfer between phases. This option considers both phases as interpenetrating continua and does not track the particles in space and time, although it constitutes a simpler and more straight forward approach to address the problem.

To test and validate both models the selective capture of hexavalent

chromium in aqueous samples into amino-functionalized magnetic particles has been selected as case study. The experimental validation has been proven successful, with relatively higher deviations in the case of the Euler-Euler option. However, the two models are equally precise when it comes to predict the chromium (VI) removal in the proximity of chemical equilibrium. A set of simulations has been run to analyze the effect of taking into account the discrete nature of the particles, showing that it becomes crucial when managing data in the kinetic region. Moreover, the divergence between models turns more significant when the concentration of particles in the system is risen.

Hence, herein we provide two valuable tools to predict the capture behavior of target species in multiphase microfluidic systems. The Euler-Euler alternative constitutes a versatile tool to assist in the prediction of the capture of the system when fast and raw data are required, being most suitable when working close to chemical equilibrium. Meanwhile, the Euler-Lagrange tool proves to be a rigorous and precise platform to shape a general and detailed view of the operation of a microfluidic solid/liquid system; it considers particles fluid dynamics, intra- and interphase mass transfer and chemical reaction phenomena, presenting the possibility of being integrated with other predictive models that consider other steps such as phase separation.

## CRedit authorship contribution statement

**Gloria González-Lavín:** Writing – original draft, Visualization, Validation, Software, Methodology, Investigation, Formal analysis, Data curation, Conceptualization. **Belén García-Merino:** Writing – original draft, Validation, Data curation. **Christian Fernández-Maza:** Writing – review & editing, Software, Methodology, Conceptualization. **Eugenio Bringas:** Writing – review & editing, Methodology. **Lucía Gómez-**

**Coma:** Writing – review & editing, Methodology, Conceptualization.  
**Marcos Fallanza:** Writing – review & editing, Supervision, Software, Methodology, Formal analysis, Conceptualization.  
**Inmaculada Ortiz:** Writing – review & editing, Supervision, Resources, Funding acquisition, Formal analysis, Conceptualization.

### Declaration of competing interest

The authors declare that they have no known competing financial interests or personal relationships that could have appeared to influence the work reported in this paper.

### Data availability

Data will be made available on request.

### Acknowledgements

This work received financial assistance from two projects and two grants funded by MICIU/AEI/10.13039/501100011033. Projects PDC2022-133122-I00 and PID2021-123120OB-I00 are also financed by the European Union Next Generation EU/PRTR and ERDF/EU, respectively. Moreover, Gloria González-Lavín gratefully acknowledges grant FPU21/03297, funded in addition by ESF+. Finally, Belén García-Merino thanks grant PRE2019-089339, which is financed by ESF Investing in your future as well.

### References

- R.M. Ashour, R. El-sayed, A.F. Abdel-Magied, A.A. Abdel-khalek, M.M. Ali, K. Forsberg, A. Uheida, M. Muhammed, J. Dutta, Selective separation of rare earth ions from aqueous solution using functionalized magnetite nanoparticles: kinetic and thermodynamic studies, *Chem. Eng. J.* 327 (2017) 286–296, <https://doi.org/10.1016/j.cej.2017.06.101>.
- A. Azzouz, S.K. Kailasa, S.S. Lee, A.J. Rascón, E. Ballesteros, M. Zhang, K.-H. Kim, Review of nanomaterials as sorbents in solid-phase extraction for environmental samples, *TrAC, Trends Anal. Chem.* 108 (2018) 347–369, <https://doi.org/10.1016/j.trac.2018.08.009>.
- G. Giakissikli, A.N. Anthemidis, Magnetic materials as sorbents for metal/metalloid preconcentration and/or separation. A review, *Anal. Chim. Acta* 789 (2013) 1–16, <https://doi.org/10.1016/j.aca.2013.04.021>.
- B. García-Merino, E. Bringas, I. Ortiz, Robust system for the regenerative capture of aqueous pollutants with continuously synthesized and functionalized magnetic nanoparticles, *J. Environ. Chem. Eng.* 10 (2022), <https://doi.org/10.1016/j.jece.2022.108417>.
- B. García-Merino, E. Bringas, I. Ortiz, Fast and reliable analysis of pH-responsive nanocarriers for drug delivery using microfluidic tools, *Int. J. Pharm.* 643 (2023) 123232, <https://doi.org/10.1016/j.ijpharm.2023.123232>.
- C. Barquín, M.J. Rivero, I. Ortiz, Shedding light on the performance of magnetically recoverable TiO<sub>2</sub>/Fe<sub>3</sub>O<sub>4</sub>/rGO-5 photocatalyst. Degradation of S-metolachlor as case study, *Chemosphere* 307 (2022) 135991, <https://doi.org/10.1016/j.chemosphere.2022.135991>.
- V. Kumaravel, S. Mathew, J. Bartlett, S.C. Pillai, Photocatalytic hydrogen production using metal doped TiO<sub>2</sub>: A review of recent advances, *Appl. Catal., B* 244 (2019) 1021–1064, <https://doi.org/10.1016/j.apcatb.2018.11.080>.
- J. Gómez-Pastora, I.H. Karamelas, E. Bringas, E.P. Furlani, I. Ortiz, Numerical analysis of bead magnetophoresis from flowing blood in a continuous-flow microchannel: implications to the bead-fluid interactions, *Sci. Rep.* 9 (2019) 7265, <https://doi.org/10.1038/s41598-019-43827-x>.
- C. Fernández-Maza, M. Fallanza, L. Gómez-Coma, I. Ortiz, Performance of continuous-flow micro-reactors with curved geometries. Experimental and numerical analysis, *Chem. Eng. J.* 437 (2022) 135192, <https://doi.org/10.1016/j.cej.2022.135192>.
- J. Gómez-Pastora, C. González-Fernández, M. Fallanza, E. Bringas, I. Ortiz, Flow patterns and mass transfer performance of miscible liquid-liquid flows in various microchannels: Numerical and experimental studies, *Chem. Eng. J.* 344 (2018) 487–497, <https://doi.org/10.1016/j.cej.2018.03.110>.
- C. Fernández-Maza, G. González-Lavín, L. Gómez-Coma, M. Fallanza, I. Ortiz, High performance flow-focusing droplet microreactor. Extractive separation of rare earths as case of study, *Chem. Eng. J.* 486 (2024) 150136, <https://doi.org/10.1016/j.cej.2024.150136>.
- O. Mahian, L. Kolsi, M. Amani, P. Estellé, G. Ahmadi, C. Kleinstreuer, J.S. Marshall, M. Siavashi, R.A. Taylor, H. Niazmand, S. Wongwises, T. Hayat, A. Kolanjiyil, A. Kasaiean, I. Pop, Recent advances in modeling and simulation of nanofluid flows-Part I: Fundamentals and theory, *Phys. Rep.* 790 (2019) 1–48, <https://doi.org/10.1016/j.physrep.2018.11.004>.
- A.V. Minakov, A.S. Lobasov, D.V. Guzei, M.I. Pryazhnikov, V.Y. Rudyak, The experimental and theoretical study of laminar forced convection of nanofluids in the round channel, *Appl. Therm. Eng.* 88 (2015) 140–148, <https://doi.org/10.1016/j.applthermaleng.2014.11.041>.
- A. Albojajmal, K. Vafai, Analysis of single phase, discrete and mixture models, in predicting nanofluid transport, *Int. J. Heat Mass Transf.* 114 (2017) 225–237, <https://doi.org/10.1016/j.ijheatmasstransfer.2017.06.030>.
- L.S. Maganti, P. Dhar, T. Sundararajan, S.K. Das, Particle and thermohydraulic maldistribution of nanofluids in parallel microchannel systems, *Microfluid. Nanofluidics* 20 (2016) 109, <https://doi.org/10.1007/s10404-016-1769-3>.
- S.A. Khashan, E.P. Furlani, Effects of particle-fluid coupling on particle transport and capture in a magnetophoretic microsystem, *Microfluid. Nanofluidics* 12 (2012) 565–580, <https://doi.org/10.1007/s10404-011-0898-y>.
- A.K. Thakur, R. Kumar, N. Banerjee, P. Chaudhari, G.K. Gaurav, Hydrodynamic modeling of liquid-solid flow in polyolefin slurry reactors using CFD techniques – A critical analysis, *Powder Technol.* 405 (2022) 117544, <https://doi.org/10.1016/j.powtec.2022.117544>.
- R.I. Singh, A. Brink, M. Hupa, CFD modeling to study fluidized bed combustion and gasification, *Appl. Therm. Eng.* 52 (2013) 585–614, <https://doi.org/10.1016/j.applthermaleng.2012.12.017>.
- S. Li, Y. Zhuo, Y. Shen, Modelling of multiphase reactive flows in a full-loop coal-direct chemical looping combustor, *Chem. Eng. J.* 457 (2023) 141306, <https://doi.org/10.1016/j.cej.2023.141306>.
- L. Yang, C. Han, J. Xu, B. Lu, Y. Xu, W. Wang, W. Ge, Role of mesoscale structure in gas–solid fluidization: Comparison between continuum and discrete approaches, *Chem. Eng. J.* 454 (2023), <https://doi.org/10.1016/j.cej.2022.139979>.
- S.M. Amin Arefi, C.W. Tony Yang, D.D. Sin, J.J. Feng, Simulation of nanoparticle transport and adsorption in a microfluidic lung-on-a-chip device, *Biomicrofluidics* 14 (2020), <https://doi.org/10.1063/5.0011353>.
- M. Gracka, R. Lima, J.M. Miranda, S. Student, B. Melka, Z. Ostrowski, Red blood cells tracking and cell-free layer formation in a microchannel with hyperbolic contraction: A CFD model validation, *Comput. Methods Programs Biomed.* 226 (2022) 107117, <https://doi.org/10.1016/j.cmpb.2022.107117>.
- L. Marocco, Modeling of the fluid dynamics and SO<sub>2</sub> absorption in a gas-liquid reactor, *Chem. Eng. J.* 162 (2010) 217–226, <https://doi.org/10.1016/j.cej.2010.05.033>.
- F. Durst, D. Milojevic, B. Schönung, Eulerian and Lagrangian predictions of particulate two-phase flows: a numerical study, *Appl. Math. Model.* 8 (1984) 101–115, [https://doi.org/10.1016/0307-904X\(84\)90062-3](https://doi.org/10.1016/0307-904X(84)90062-3).
- M. Adnan, J. Sun, N. Ahmad, J.J. Wei, Verification and validation of the DDPM-EMMS model for numerical simulations of bubbling, turbulent and circulating fluidized beds, *Powder Technol.* 379 (2021) 69–88, <https://doi.org/10.1016/j.powtec.2020.10.041>.
- H. Pouraria, F. Darihaki, K.H. Park, S.A. Shirazi, Y. Seo, CFD modelling of the influence of particle loading on erosion using dense discrete particle model, *Wear* 460–461 (2020) 203450, <https://doi.org/10.1016/j.wear.2020.203450>.
- Y. Xu, B. Jin, Y. Zhao, E.J. Hu, X. Chen, X. Li, Numerical simulation of aqueous ammonia-based CO<sub>2</sub> absorption in a sprayer tower: An integrated model combining gas-liquid hydrodynamics and chemistry, *Appl. Energy* 211 (2018) 318–333, <https://doi.org/10.1016/j.apenergy.2017.11.054>.
- A.K. Pukkella, R. Vysyaraju, V. Tammishetti, B. Rai, S. Subramanian, Improved mixing of solid suspensions in stirred tanks with interface baffles: CFD simulation and experimental validation, *Chem. Eng. J.* 358 (2019) 621–633, <https://doi.org/10.1016/j.cej.2018.10.020>.
- M. Ahmadzadeh, E. Farokhi, M. Shams, Investigating the effect of air conditioning on the distribution and transmission of COVID-19 virus particles, *J. Clean Prod.* 316 (2021) 128147, <https://doi.org/10.1016/j.jclepro.2021.128147>.
- T. Dbouk, D. Drikakis, On coughing and airborne droplet transmission to humans, *Phys. Fluids* 32 (2020) 053310, <https://doi.org/10.1063/5.0011960>.
- H.X. Ren, L.X. Zhang, G. Guo, Z.B. Tong, Z.Y. Li, Y. Zhang, A.B. Yu, Numerical simulation investigation of drug deposition process during nasal administration with auxiliary airflow, *Powder Technol.* 426 (2023) 118534, <https://doi.org/10.1016/j.powtec.2023.118534>.
- B.A. Wols, C.H.M. Hofman-Caris, Modelling micropollutant degradation in UV/H<sub>2</sub>O<sub>2</sub> systems: Lagrangian versus Eulerian method, *Chem. Eng. J.* 210 (2012) 289–297, <https://doi.org/10.1016/j.cej.2012.08.088>.
- J. Gómez-Pastora, I.H. Karamelas, X. Xue, E. Bringas, E.P. Furlani, I. Ortiz, Magnetic bead separation from flowing blood in a two-phase continuous-flow magnetophoretic microdevice: theoretical analysis through computational fluid dynamics simulation, *J. Phys. Chem. C* 121 (2017) 7466–7477, <https://doi.org/10.1021/acs.jpcc.6b12835>.
- P. Bhardwaj, P. Bagdi, A.K. Sen, Microfluidic device based on a microhydrocyclone for particle-liquid separation, *Lab Chip* 11 (2011) 4012–4021, <https://doi.org/10.1039/c1lc20606k>.
- A. Shiriny, M. Bayareh, Inertial focusing of CTCs in a novel spiral microchannel, *Chem. Eng. Sci.* 229 (2021) 116102, <https://doi.org/10.1016/j.ces.2020.116102>.
- J. Rostami, A. Abbassi, J. Harting, Heat transfer by nanofluids in wavy microchannels, *Adv. Powder Technol.* 29 (2018) 925–933, <https://doi.org/10.1016/j.apt.2018.01.010>.
- M. Wang, P.S. Dobson, M.C. Paul, Numerical investigation of nanofluid deposition in a microchannel cooling system, *Powder Technol.* 425 (2023) 118582, <https://doi.org/10.1016/j.powtec.2023.118582>.
- J.M.F. Oro, *Técnicas Numéricas en Ingeniería de Fluidos*, Reverté, Barcelona, 2012.
- A. Basauri, J. Gómez-Pastora, M. Fallanza, E. Bringas, I. Ortiz, Predictive model for the design of reactive micro-separations, *Sep. Purif. Technol.* 209 (2019) 900–907, <https://doi.org/10.1016/j.seppur.2018.09.028>.

- [40] Ansys® Fluent, Release 2024R1, Ansys Fluent User's Guide.
- [41] M. Charjouei Moghadam, A. Eilaghi, P. Rezai, Inertia-magnetic particle sorting in microfluidic devices: a numerical parametric investigation, *Microfluid. Nanofluidics* 23 (2019) 135, <https://doi.org/10.1007/s10404-019-2301-3>.
- [42] P. Bhardwaj, P. Bagdi, A.K. Sen, Microfluidic device based on a micro-hydrocyclone for particle-liquid separation, *Lab Chip* 11 (2011) 4012, <https://doi.org/10.1039/c1lc20606k>.
- [43] A. Li, G. Ahmadi, Dispersion and deposition of spherical particles from point sources in a turbulent channel flow, *Aerosol Sci. Technol.* 16 (1992) 209–226, <https://doi.org/10.1080/02786829208959550>.
- [44] S.A. Morsi, A.J. Alexander, An investigation of particle trajectories in two-phase flow systems, *J. Fluid Mech.* 55 (1972) 193–208, <https://doi.org/10.1017/S0022112072001806>.
- [45] K.K. Sirkar, Creeping flow mass transfer to a single active sphere in a random spherical inactive particle cloud at high Schmidt numbers, *Chem. Eng. Sci.* 29 (1974) 863–869, [https://doi.org/10.1016/0009-2509\(74\)80206-X](https://doi.org/10.1016/0009-2509(74)80206-X).
- [46] M. Sommerfeld, *Numerical Methods for Dispersed Multiphase Flows*, in: *Particles in Flows*, Birkhäuser Cham, 2017: pp. 327–396. [https://doi.org/10.1007/978-3-319-60282-0\\_6](https://doi.org/10.1007/978-3-319-60282-0_6).
- [47] U. Jeong, H.H. Shin, Y. Kim, Functionalized magnetic core-shell Fe@SiO<sub>2</sub> nanoparticles as recoverable colorimetric sensor for Co<sup>2+</sup> ion, *Chem. Eng. J.* 281 (2015) 428–433, <https://doi.org/10.1016/j.cej.2015.07.006>.
- [48] Y. Yang, Y. Zhang, J.C. Shen, H. Yang, Z.G. Zhou, S.P. Yang, A highly selective magnetic sensor with functionalized Fe/Fe<sub>3</sub>O<sub>4</sub> nanoparticles for detection of Pb<sup>2+</sup>, *Chin. Chem. Lett.* 27 (2016) 891–895, <https://doi.org/10.1016/j.ccllet.2016.01.060>.
- [49] J. Gómez-Pastora, E. Bringas, I. Ortiz, Recent progress and future challenges on the use of high performance magnetic nano-adsorbents in environmental applications, *Chem. Eng. J.* 256 (2014) 187–204, <https://doi.org/10.1016/j.cej.2014.06.119>.
- [50] E. Bringas, J. Saiz, I. Ortiz, Removal of As(V) from groundwater using functionalized magnetic adsorbent materials: Effects of competing ions, *Sep. Purif. Technol.* 156 (2015) 699–707, <https://doi.org/10.1016/j.seppur.2015.10.068>.
- [51] L. Wu, A. Mendoza-Garcia, Q. Li, S. Sun, *Organic Phase Syntheses of Magnetic Nanoparticles and Their Applications*, *Chem. Rev.* 116 (2016) 10473–10512, <https://doi.org/10.1021/acs.chemrev.5b00687>.
- [52] Z. Chen, C. Wu, Z. Zhang, W. Wu, X. Wang, Z. Yu, Synthesis, functionalization, and nanomedical applications of functional magnetic nanoparticles, *Chin. Chem. Lett.* 29 (2018) 1601–1608, <https://doi.org/10.1016/j.ccllet.2018.08.007>.
- [53] B. García-Merino, E. Bringas, I. Ortiz, Synthesis and applications of surface-modified magnetic nanoparticles: Progress and future prospects, *Rev. Chem. Eng.* 38 (2021) 821–842, <https://doi.org/10.1515/revce-2020-0072>.
- [54] C. González Fernández, J. Gómez-Pastora, A. Basauri, M. Fallanza, E. Bringas, J. J. Chalmers, I. Ortiz, Continuous-flow separation of magnetic particles from biofluids: how does the microdevice geometry determine the separation performance? *Sensors* 20 (2020) 3030, <https://doi.org/10.3390/s20113030>.
- [55] J. Gómez-Pastora, C. González-Fernández, E. Real, A. Iles, E. Bringas, E.P. Furlani, I. Ortiz, Computational modeling and fluorescence microscopy characterization of a two-phase magnetophoretic microsystem for continuous-flow blood detoxification, *Lab Chip* 18 (2018) 1593–1606, <https://doi.org/10.1039/c8lc00396c>.
- [56] M. Despotovic, V. Nedic, D. Despotovic, S. Cvetanovic, Evaluation of empirical models for predicting monthly mean horizontal diffuse solar radiation, *Renew. Sustain. Energy Rev.* 56 (2016) 246–260, <https://doi.org/10.1016/j.rser.2015.11.058>.